ELSEVIER

Journal of Nuclear Materials 305 (2002) 175–186

journal of nuclear materials

www.elsevier.com/locate/jnucmat

Thermal creep of Zr–Nb1%–O alloys: experimental analysis and micromechanical modelling

R. Brenner [a,b,*], J.L. Béchade [b], O. Castelnau [a], B. Bacroix [a]

[a] *LPMTM-CNRS, Université Paris-Nord, 93430 Villetaneuse, France*
[b] *CEA-DEN/SRMA, CEA Saclay, 91191 Gif-sur-Yvette cedex, France*

Received 27 January 2002; accepted 8 July 2002

Abstract

Zirconium alloys present a large variability of their mechanical behaviour with respect not only to their chemical composition but also to their microstructure. We analyze here the creep behaviour at 400 °C of two Zr–Nb1%–O alloys presenting identical chemical composition, crystallographic texture, grain size and grain shape. Both alloys *only* differ by the thermal cycles imposed during the fabrication process, either below (alloy A) or alternatively above and below (alloy B) the monotectoïd transition. This sole difference gives rise to creep rates varying by a factor of about 4 between the two alloys. From a microstructural point of view, alloys A and B differ by the precipitates distribution and the thermodynamical state (alloy B is in a metastable equilibrium state). Our experimental analysis based on mechanical tests, transmission electron microscopy (TEM) observations and phase analysis by X-ray diffraction strongly suggests an hardening effect of Nb in solid solution to explain the differences between alloys A and B. This result is confirmed by TEM X-ray spectrometry which gives a weight content of Nb in solid solution differing by about 0.1% between the two alloys. A predictive micromechanical model, based on the self-consistent affine scheme, is then applied. This model well captures the anisotropy of the specimens, and describes accurately both transient and secondary creep regimes. As a result of the identification procedure, identical hardening laws are obtained for the two alloys at the grain scale, and the saturating reference stress for prismatic slip is found to be higher for alloy B by about 30 MPa with respect to alloy A.

1. Introduction

Zirconium alloys, which are widely used in the nuclear industry especially as cladding tubes and guide tubes for pressurized water reactors, can present a variability of their thermomechanical behaviour (e.g. thermal creep) as a function not only of the chemical composition but also of the microstructure. For a better control of the mechanical behaviour of the actual alloys, but also to take into account the evolution of the industrial elaboration processes (chemical composition, thermal treatments, etc.), different studies have been engaged, for instance [1,2], to build a predictive modelling aiming at a precise description of the relationship between microstructure and effective mechanical behaviour. Following recent studies [3] on the optimization of the M5™ cladding tubes made of ternary alloy (Zr–Nb–O), this paper deals with the understanding of the influence of the microstructure on the thermal creep behaviour of Zr–Nb1%–O alloys at 400 °C. We have worked on fully annealed cladding tubes issued from the same ingot (i.e. same chemical composition) but elaborated using two different thermomechanical treatments which mainly differ by the time spent above the monotectoïd transformation (620 °C). These two thermomechanical treatments give rise to two different types of

* Corresponding author. Address: LPMTM-CNRS, Université Paris-Nord, 93430 Villetaneuse, France. Tel.: +33-1 49 40 34 68; fax: +33-1 49 40 39 38.
E-mail address: rb@galilee.univ-paris13.fr (R. Brenner).

0022-3115/02/$ - see front matter
PII: S0022-3115(02)00923-6

microstructure which apparently mainly differ by the spatial repartition of precipitates. The two alloys are found to exhibit significantly different viscosities under creep loading. Based on an experimental analysis coupled with an homogenization approach, this study contributes (i) to analyze and understand the observed differences on the mechanical behaviour and (ii) to establish a predictive modelling of the thermal creep, based on a physically relevant averaged constitutive relation at the grain scale and an accurate scale-transition scheme.

2. Investigated material

2.1. Elaboration

The products used for this study are Zr–Nb1%–O cladding tubes. All tubes are issued from the same ingot (i.e. same chemical composition, Table 1) and were obtained with identical cold-rolling operations (i.e. identical number of passes and reduction ratio). They *only* differ by the intermediate heat treatments performed during the cold-rolling process. According to the Zr–Nb phase diagram [4], a monotectoïd transformation $\beta\text{-Zr} \leftrightarrow \alpha\text{-Zr} + \beta\text{-Nb}$ takes place at about 620 °C, where β-Zr and β-Nb are body centered cubic (bcc) phases respectively rich in Zr (∼80%) and Nb (∼90%) whereas α-Zr is an hexagonal close-packed (hcp) phase containing up to 0.6 wt% niobium. These different phases do not involve other chemical elements than Zr and Nb. Note that the α-Zr phase exists up to ∼863 °C. It is thus possible to perform the intermediate recrystallization treatments either in the 'high-temperature' domain ($\alpha\text{-Zr} + \beta\text{-Zr}$) or in the 'low-temperature' domain ($\alpha\text{-Zr} + \beta\text{-Nb}$). We focused on two particular heat treatment processes schematically described in Fig. 1. In one case, all heat treatments are performed below the monotectoïd temperature at 580 °C whereas in the other case they alternate above and below the monotectoïd plateau. In what follows, the resulting products will be referred, respectively, as alloy A and alloy B.

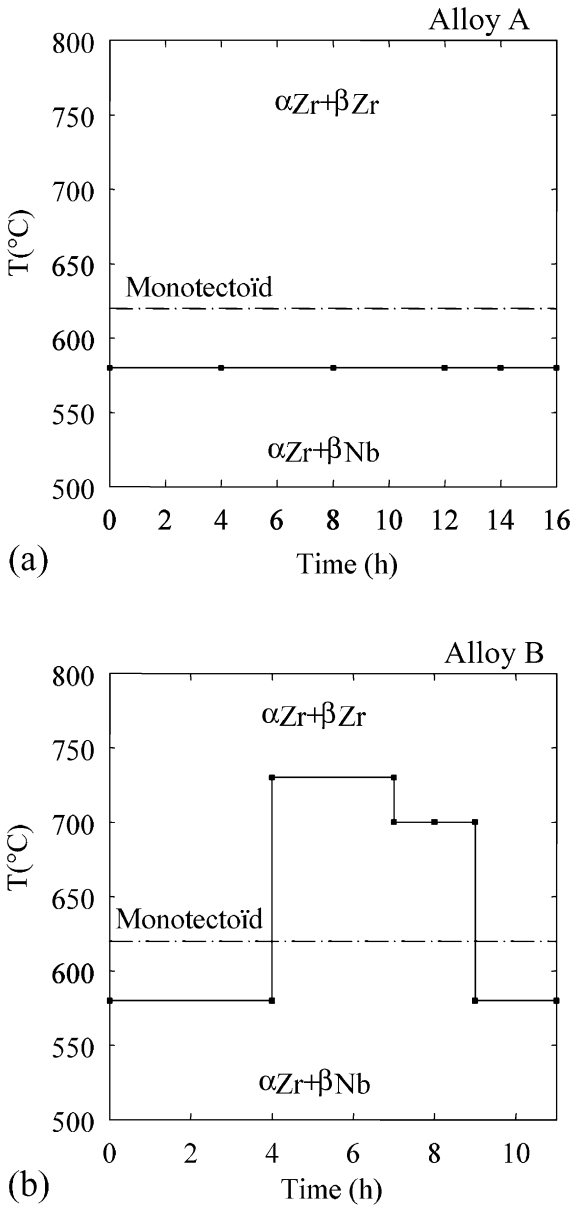

Fig. 1. Intermediate recrystallization heat treatments of Zr–Nb1%–O alloys during the elaboration process at (a) low- and (b) mixed-temperature.

2.2. Texture and microstructure

The orientation distribution function, characterizing the crystallographic texture of the two alloys, has been calculated from 5 experimental pole figures obtained by X-ray diffraction using the Cu Kα radiation. As shown in Fig. 2, the two alloys present identical textures which are characterized by a maximum density of $\{11\bar{2}0\}$ poles along the axial direction of the tube (AD) and a spread of the $\{0002\}$ poles in the radial-tangential plane with a maximum density located at about 30° of the radial direction (RD). This texture corresponds to recrystallized tubes obtained with a thickness reduction greater than the diameter reduction during the cold-rolling process (i.e. ratio $Q > 1$, see [5]).

Table 1
Chemical composition of Zr–Nb1%–O alloy (wt ppm except where indicated)

Nb	O	Fe	S	Zr
1%	1100	300	$\leqslant 10$	Balance

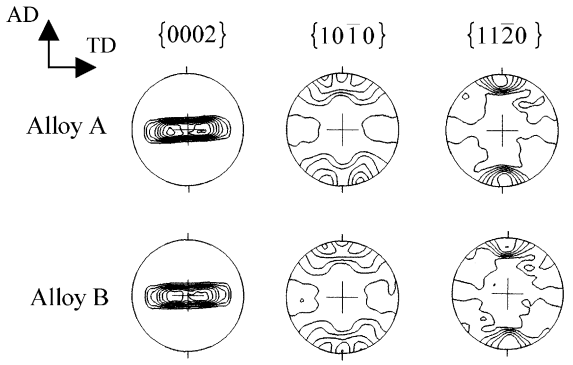

Fig. 2. Crystallographic texture of the alloys A and B. Pole figures recalculated with the harmonic method. Density level: 1–1.5–2... (random units), AD: axial direction, TD: transverse direction.

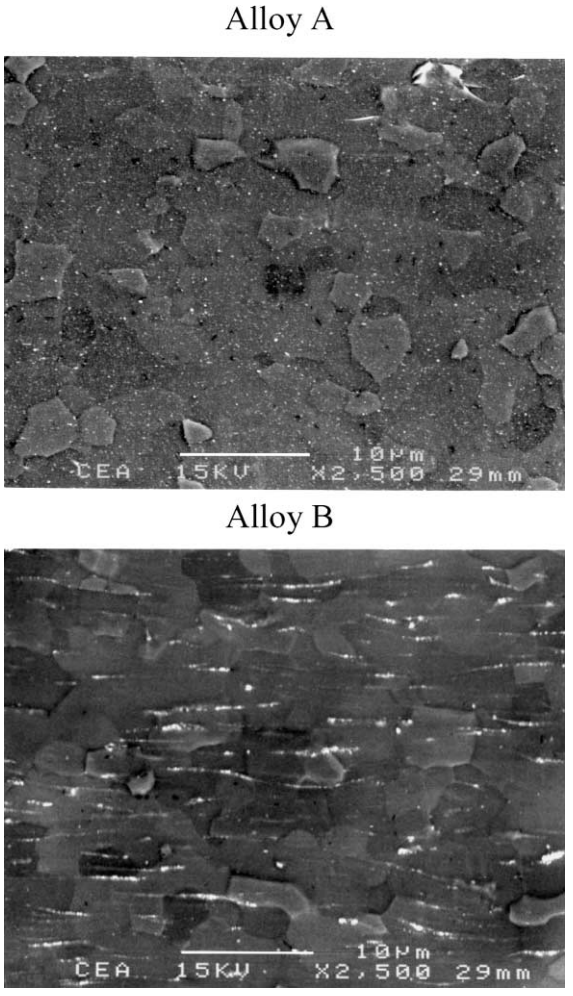

Fig. 3. Microstructure of the Zr–Nb1%–O alloys A and B.

The observation of the alloys by optical microscopy reveals in both cases a homogeneous grain size (α-Zr phase) of about 5 μm. The repartition of the β-Nb precipitates has been observed using scanning electron microscopy (Fig. 3). It can be seen that the two materials differ strongly with respect to the distribution of the β-Nb phase. Alloy A presents a homogeneous repartition of the precipitate phase due to the heat treatments performed below the monotectoïd temperature, which is the domain of equilibrium between room temperature and 620 °C. On the contrary, alloy B presents an heterogeneous distribution of the precipitates which are aligned along the cold-rolling direction. This can be explained by the 'high temperature' heat treatment in the α-Zr + β-Zr domain during which the β-Zr phase nucleates on the grain boundaries of the α-Zr phase and is further retained during cooling. Consequently, the following cold-rolling operation will lead to the alignment of this phase along the axial (rolling) direction. It can be noted that these alignments are transgranular aggregates of precipitates. In both alloys, the precipitates size is about 50 nm.

3. Influence of the microstructure on thermal creep behaviour

The creep response of the Zr–Nb1%–O alloy was investigated at 400 °C in the low-stress domain (i.e. below the yield strength). Indeed, these stress-temperature conditions correspond to the one used industrially to characterize the out-of-pile creep behaviour. In this context, the response to an *internal pressure* loading with a hoop stress $\sigma_{\theta\theta} = 130$ MPa was first studied. As reported in Fig. 4, the evolution of the effective hoop strain during creep clearly indicates a strong dependence on the microstructure of the material. In the steady-state regime, alloy B deforms much more slowly and presents a hoop strain rate as little as four times lower than alloy A. Note that the same ratio has been obtained for other stress levels [1], not reported here for brevity. On the other hand, the stress sensitivity n ($n = \Delta \log \dot{\varepsilon} / \Delta \log \sigma$) is found identical for the two alloys and equal to 4 in this low-stress domain. This tends to indicate that the deformation mechanisms are the same in both alloys but that their kinetic strongly differs. We will now investigate which microstructural factor is responsible for these different behaviours.

3.1. Role of the precipitate distribution

One could first incriminate the different precipitate distributions to explain the different mechanical behaviour. According to this, the morphology of alloy B being strongly anisotropic, a directional effect of the microstructural hardening could be expected. *Uniaxial* creep tests were thus performed in the axial and hoop

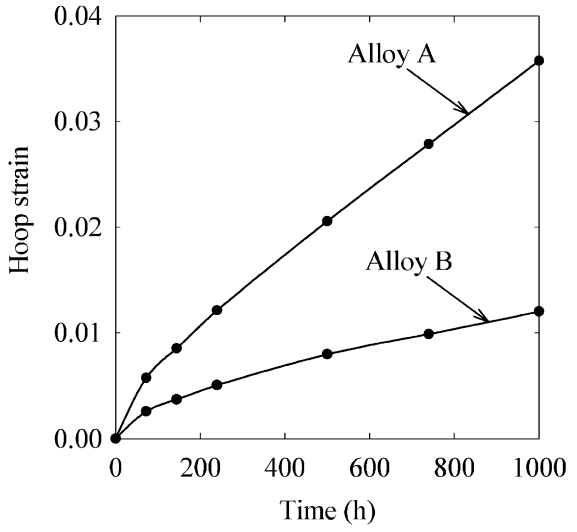

Fig. 4. Hoop strain evolution during an internal pressure creep test ($T = 400$ °C, $\sigma_{\theta\theta} = 130$ MPa) for alloys A and B.

directions for both alloys. The results reported in Fig. 5 show that the hardening effect is independent on the loading direction. On the other hand, a ratio of 4 is still obtained between the steady-state strain rates of the two alloys, for the two loading directions, i.e. similar to that obtained for internal pressure loading. It can thus be concluded that the hardening observed between both alloys is not due to a morphological effect of the repartition of the β phase. Furthermore, it must be recalled that these materials present a pronounced crystallographic texture (Fig. 2). Consequently, owing to the strong plastic anisotropy of the hcp single crystal (see for instance [6]), different slip systems will be activated with varying loading paths. With respect to this observation, the independence of the strain rate ratio in the steady-state regime for different loading directions indicates that the observed hardening affects identically all the slip systems of the crystalline structure. Finally, tests at different stress levels allowed us to determine the stress sensitivity n for the two uniaxial loading; a value of 6 was found for the axial direction and of 5 for the hoop direction. Obviously, these results imply, for the single crystal behaviour, different stress sensitivity coefficients for different slip systems.

Following this macroscopic characterization, refined observations were performed at the dislocation scale to study the influence of the precipitates distribution on the dislocation microstructure. Both alloys, after deformation under internal pressure creep tests (plastic strain less than 5%), were observed by transmission electron microscopy (TEM). Due to the tubular geometry and the small thickness (0.6 μm), only thin foils perpendicular to the radial direction could be obtained. Consequently, with respect to the crystallographic texture, the plane of the thin foils is close to the basal plane. Representative dislocation microstructures are reported in Fig. 6. In both specimens, we observed 2–3 slip systems per grain. The systems activated are similar in both alloys, mainly prismatic $(\mathrm{P}\langle\mathbf{a}\rangle)\{1\,0\,\bar{1}\,0\}\langle 1\,\bar{2}\,1\,0\rangle$ and pyramidal $\langle\mathbf{a}\rangle(\Pi_1\langle\mathbf{a}\rangle)\{1\,0\,\bar{1}\,1\}\langle 1\bar{2}10\rangle$. Two others slip systems, namely basal $(\mathrm{B}\langle\mathbf{a}\rangle)\{0\,0\,0\,2\}\langle 1\,\bar{2}\,1\,0\rangle$ and pyramidal $\langle\mathbf{c}+\mathbf{a}\rangle(\Pi_1\langle\mathbf{c}+\mathbf{a}\rangle)\{1\,0\,\bar{1}\,1\}\langle\bar{2}\,1\,1\,3\rangle$, were observed sporadically. Besides, no cell structures were observed. In alloy A, the dislocation density is relatively uniform and the dislocations are often pinned by the precipitates. On contrary, in alloy B, the major part of each grain is

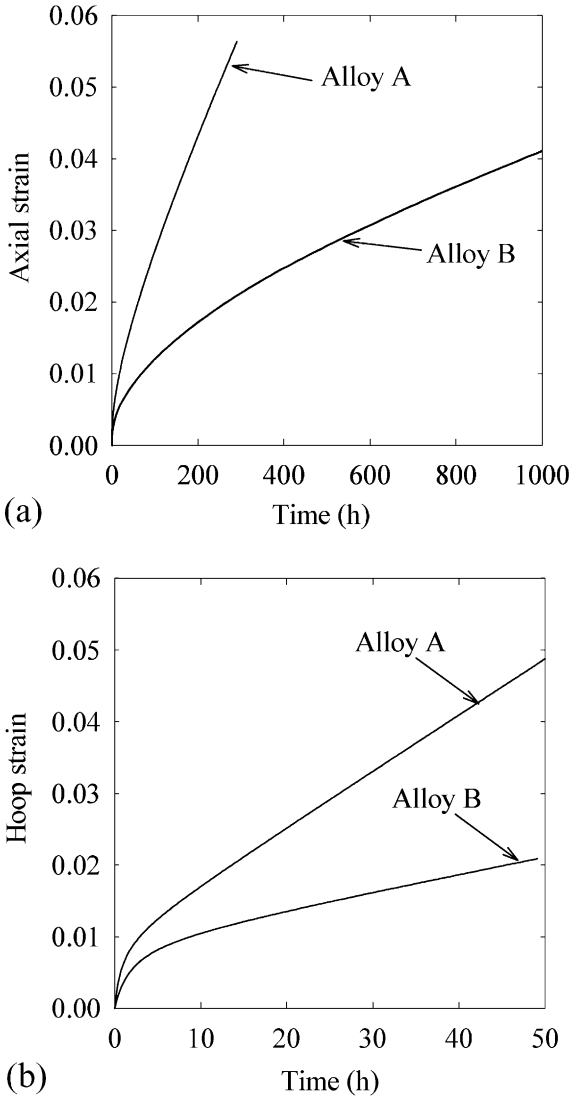

Fig. 5. Strain evolution during uniaxial creep tests in (a) the axial direction ($T = 400$ °C, $\sigma_{zz} = 113$ MPa) and (b) the hoop direction ($T = 400$ °C, $\sigma_{\theta\theta} = 160$ MPa) for alloys A and B.

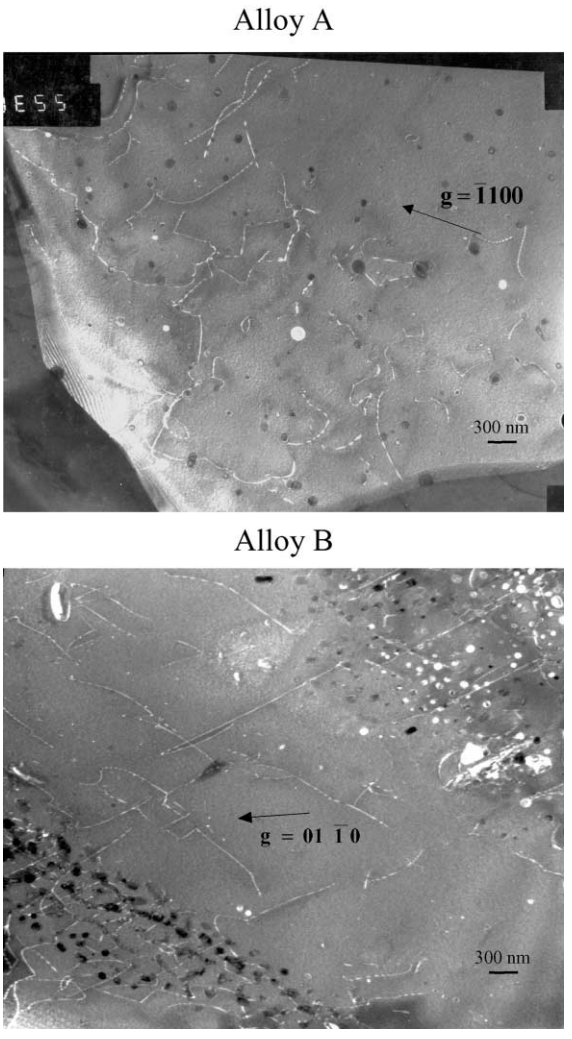

Fig. 6. Dislocation microstructures observed after internal pressure creep test ($T = 400$ °C, $\sigma_{\theta\theta} = 130$ MPa, 1000 h) for both alloys.

constituted by precipitates-free zones where the dislocation density appears to be lower than in the alignments of β-Nb phase. Regarding these observations, a structural hardening mechanism cannot be invoked to explain the creep behaviour of Zr–Nb1%–O alloys since the dislocations interacts mainly with the precipitates in alloy A. It can thus be deduced that these interactions are not the mechanism controlling the deformation in the studied creep regime.

3.2. Role of the solid solution

Following these results, it is necessary to go back to the differences in the heat treatment process of the two alloys. As shown above, the main difference is that alloy B was heat treated in the α-Zr + β-Zr domain during its elaboration. Recent studies [7] for these different elaboration processes have shown that the β-Zr phase has a very slow transformation kinetic during cooling and can thus be retained in a metastable state at room temperature, which was also previously reported for other Zr–Nb alloys [8]. Further heat treatments below the monotectoïd plateau are thus required for the alloy to recover its equilibrium state. Consequently, the important parameter to characterize the thermodynamical state of the alloy is the cumulated time of heat treatments below the monotectoïd temperature *since* the last treatment in the α-Zr + β-Zr domain. Fig. 1 indicates that this cumulated time is 16 h for alloy A whereas it is only of 2 h for alloy B. Note that, due to the slow precipitation kinetic of the β-Nb phase especially at low temperature ($T < 500$ °C), this difference of heat treatments is significant, in terms of thermodynamical state, compared to the duration of a creep test (1000 h) at 400 °C. According to the results obtained in [7], alloy A can be considered in a quasi-equilibrium state whereas alloy B is in a metastable state. In other words, due to the difference in the nature of the β phases in the alloy either rich in Zr or in Nb and their respective volume fraction, the two alloys are likely to present at room temperature different Nb contents in the solid solution of the α-Zr phase. This last point will now be investigated. Since small variations of the Nb content of the α-Zr phase are expected, we tackle this analysis in two ways.

3.2.1. Volume fraction of β-Nb phase

First, the study is focused on the volume fraction of the β-Nb phase in the two materials. It is expected to be linked to the Nb content of the α-Zr since an increasing fraction of β-Nb corresponds to a decreasing Nb content in the matrix. The volume fraction of β-Nb in both alloys in their initial states (i.e. before creep test) has been investigated by the analysis of the integrated intensity of an X-ray diffraction peak profile corresponding to the β-Nb phase. Due to the small volume fraction of the β-Nb phase, we could only study the diffraction peak profile corresponding to the $\{1\,1\,0\}$ plane. Nevertheless, it is reasonable to assume that the precipitates in the material do not present a particular crystallographic texture. Consequently, the study can be restricted to only one peak. As shown in Fig. 7, the $\{1\,1\,0\}$β-Nb line is clearly defined for alloy A whereas it is quasi undistinguishable for alloy B. These results confirm the expected difference in the thermodynamical state. Alloy B is in a metastable state and, after deconvolution and subtraction of the background, one obtains a volume fraction of β-Nb phase 4 times lower than for alloy A. To validate the relation between the β-Nb volume fraction and the thermodynamical state of the alloy, a subsequent heat treatment was made for alloy B ($T = 570$ °C during 1000 h) in order to obtain an evolution towards the equilibrium state. Fig. 8 shows the evolution of the β-Nb

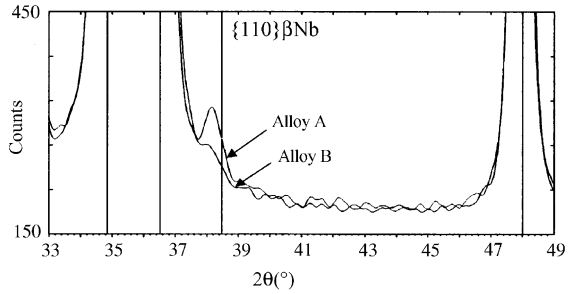

Fig. 7. {110}β-Nb peak of the X-ray diffraction spectrum associated to the initial state of alloys A and B.

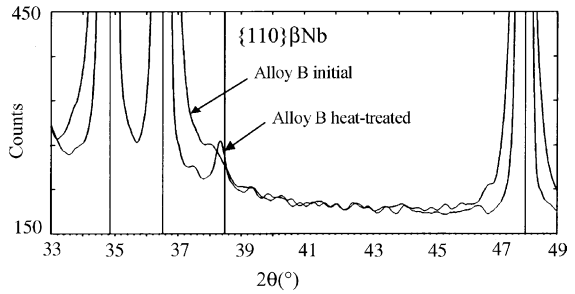

Fig. 8. {110}β-Nb peak of the X-ray diffraction spectrum associated to the initial and heat-treated states of alloy B.

content before and after the heat treatment. The increase of the β-Nb volume fraction confirms the evolution of alloy B towards an equilibrium state. Nevertheless, the integrated intensity after the heat treatment remains lower than the one of alloy A. It can be thought that the heat treatment was not long enough to attain a 'real' equilibrium state. This last remark implies that, according to the thermodynamical state, we now have three different materials (initial alloys A and B and heat-treated alloy B). An internal pressure creep test was thus performed on the heat-treated alloy B. Fig. 9 shows the comparison of the creep responses of the three materials. It is observed that the heat treatment of alloy B leads to an increase of the creep strain rate. This emphasizes the influence of the thermodynamical state of the alloy on its creep behaviour. Furthermore, combining the X-ray analysis and the creep responses, it was found that the logarithm of the steady-state strain rate increases approximately linearly with the integrated intensity of the {110}β-Nb diffraction peaks which is proportional to the β-Nb volume fraction (Fig. 10).

3.2.2. Nb content in α-Zr phase

To assess the link between the Nb content in the α-Zr phase and the β-Nb volume fraction, a direct analysis of the Nb content in the matrix was performed by TEM X-ray spectrometry. The measures were made on different

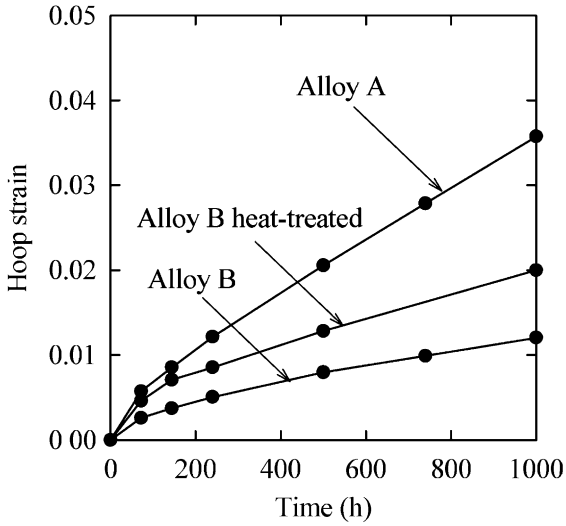

Fig. 9. Hoop strain evolution during an internal pressure creep test ($T = 400$ °C, $\sigma_{\theta\theta} = 130$ MPa) for alloys A and B in their initial state and heat-treated alloy B.

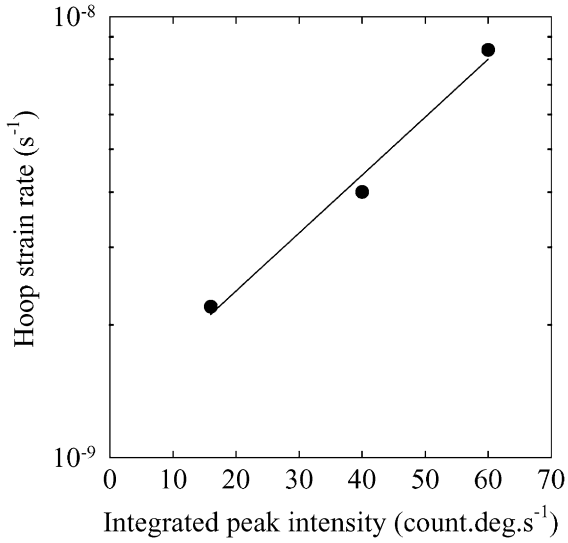

Fig. 10. Hoop strain rate of Zr–Nb-1%O alloy as a function of the integrated intensity of the {110}β-Nb diffraction peaks.

thin foils randomly taken in the cladding tubes. As shown in Fig. 11, it was necessary to sum a very large number of spectra to obtain a stabilized value in both cases. It is worth noting that the searched difference in Nb content between the two alloys is likely to be close to the resolution of the experimental setup (about 0.1%). Nevertheless, the results reported in Fig. 11 were found to be reproducible. They indicate an higher Nb content in the α-Zr phase for alloy B with a difference of about

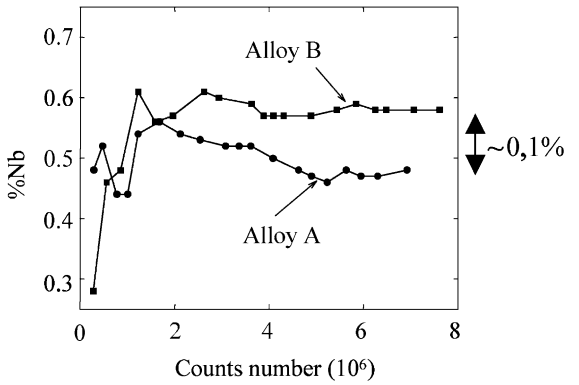

Fig. 11. Nb content measured in the α-Zr phase by X-ray spectrometry as a function of the number of counts for alloys A and B.

0.1%. It is important to note that such a trend is fully consistent with the results obtained by the X-ray diffraction analysis of the β-Nb phase. This confirms that a direct link can be made between the Nb content of the α-Zr phase and the volume fraction of the β-Nb. At this point of the experimental analysis, all our results thus converge to the predominant role of an excess of Nb in the α-Zr solid solution.

Solid solution hardening can involve mobile or immobile solute atoms interacting with dislocations. To check this point, uniaxial tensile tests under different strain rates were performed. As shown in Fig. 12, the hardening effect strongly depends on the strain rate. The stress level *difference* between both alloys increases with a decrease of the strain rate (equivalent to an increase of the temperature). This observation excludes the possibility of immobile Nb atoms interacting with dislocations. Indeed, the different models proposed in that framework by Friedel [9] or Fleisher [10] imply an increase of the hardening effect with an increase of the strain rate. Furthermore, these models predict an overestimated hardening of not more than 20 MPa at 0 K. Therefore, our results strongly suggest a hardening mechanism involving mobile solute Nb atoms. The detailed study of this hardening mechanism requires further experimental analysis and is beyond the scope of this paper.

3.3. Synthesis

We have analyzed the influence of the microstructure on the thermal creep behaviour of Zr–Nb1%–O alloys presenting varying heat treatment conditions during the elaboration. It has been shown that this variability in the process results in a variability in the distribution of the β phase in the material and leads to different thermodynamical states of the alloy. The following features are worth to be recalled:

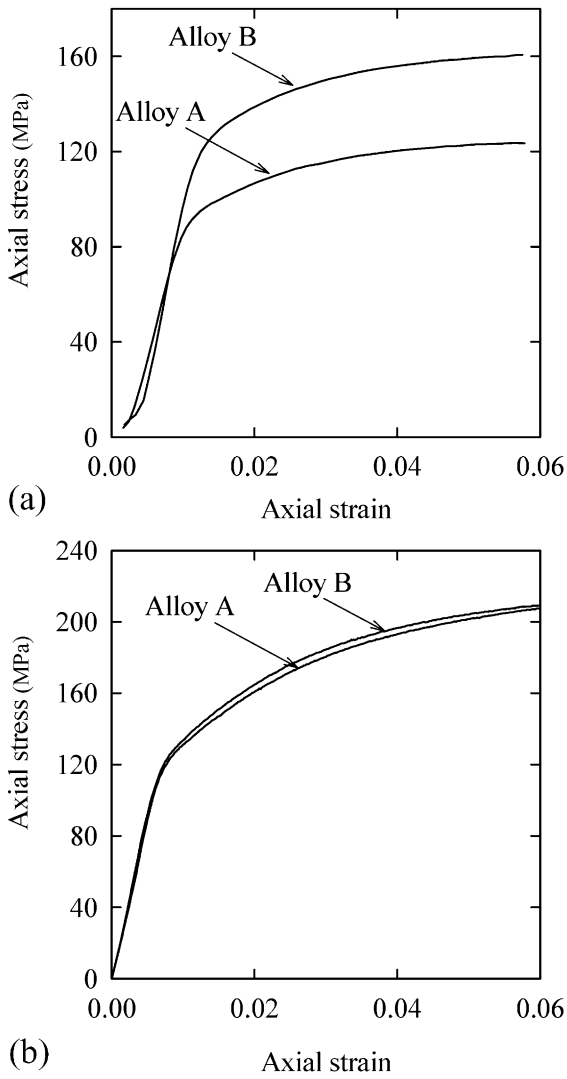

Fig. 12. Uniaxial response of alloys A and B for tensile tests along AD performed at (a) $\dot{\varepsilon} = 4 \times 10^{-7}$ s^{-1} and (b) $\dot{\varepsilon} = 2.5 \times 10^{-4}$ s^{-1}.

- the precipitates distribution is not responsible for the observed hardening effect. Dislocation–precipitates interactions are present in the alloy but they do not constitute the rate controlling deformation mechanism,
- the variation of the steady-state creep strain rate is correlated to the β-Nb volume fraction and thus to the Nb content in the α-Zr matrix. This strongly suggests a solid solution hardening mechanism. A difference about 0.1% of Nb content in the α-Zr phase was found between the two studied alloys,
- the hardening seems to modify the kinetic of the deformation mechanisms but does not change their nature, particularly, no differences were observed on the

activated slip systems between both alloys for a given loading path.

Following these experimental observations, an homogenization scheme was used to estimate the elastoviscoplastic response of Zr–Nb1%–O alloys from their local behaviour. In the next section, the model is briefly presented and the results obtained both in terms of local parameters and prediction of the effective behaviour are discussed.

4. Elastoviscoplastic micromechanical modelling

The homogenization techniques aim at deriving the effective behaviour of heterogeneous materials from the behaviour of their elementary constituents using appropriate average operators. Such an approach is thus well adapted to deal with the relation between microstructure and effective properties. For a comprehensive discussion of this approach in the framework of polycrystals, refer to [11,12].

In the sequel, the Zr–Nb1%–O polycrystals will be considered as composite materials. Assuming that the material is made of randomly distributed grains with an equiaxed shape (i.e. fully recrystallized state), an ensemble of grains with the same crystallographic orientation defines a *phase* with a given volume fraction. The distribution of phases within the polycrystal is assumed to be close to that considered in the self-consistent model, i.e. a 'random distribution', with a spherical distribution so that the phase average stress and strain fields can be calculated by means of the Eshelby inclusion problem [13]. It is worth noting that within this scheme, stress and strain fields are *not* assumed to be homogeneous within the phases, as often written in the literature. To deal with creep responses, an elastoviscoplastic behaviour has to be considered for the phases, and the scale-transition scheme has to be able to retain the 'long range memory effect' associated to the elastoviscoplastic coupling that appears in the transient regime [14]. Without going further into details, we emphasize that use is made here of an 'affine-type' formulation which respects these requirements and allows a very efficient numerical resolution. The adopted model is based on the works of Masson and Zaoui [15] and Pouya and Zaoui [16], and it is described in details in [17]. The formulation of this approach is briefly recalled in Appendix A. In the present section, we mainly pay attention to the description of the considered local constitutive behaviour. It is stressed that the elementary scale at which the local behaviour is defined here is an ensemble of grains. The local constitutive relation is thus *necessarily* phenomenological, independently on its form, with respect to the dislocation scale at which the microstructural effects, seen in Section 3, happen.

4.1. Description of the local viscoplastic flow

To describe the dislocation glide in the creep regime studied, a quite simple power-law type relation is adopted with an hyperbolic sine dependence as proposed in [18]. This description is expected to be adapted to our analysis since it is restricted to one temperature level and explores a relatively small stress domain. Furthermore, even if the affine linearization procedure is at present one of the most elaborated for dealing with elastoviscoplastic behaviour, still rather crude approximations have to be made to obtain (A.3), see [17], so that the use of a more 'physically based' constitutive relation is not believed to provide more informations concerning the physical processes of the deformation. For a given slip system (s), the slip rate $\dot{\gamma}_s$ thus reads

$$\dot{\gamma}_s = \dot{\gamma}_s^0 \left(\sinh\left(\frac{\tau_s}{\tau_s^0} \right) \right)^{n^s} \tag{1}$$

with $\dot{\gamma}_s^0$ the reference slip rate, τ_s^0 the reference shear stress and n^s the stress sensitivity of system (s). The resolved shear stress is defined as $\tau_s = \mathbf{R}_s : \boldsymbol{\sigma}$, where the Schmid tensor $\mathbf{R}_s = (\mathbf{n}_s \otimes \mathbf{m}_s + \mathbf{m}_s \otimes \mathbf{n}_s)/2$ characterizes the orientation of the slip system (s) ($\mathbf{n}_s$ and $\mathbf{m}_s$ are the unit vectors normal to the slip plane and along the slip direction). According to the kinematics of plasticity, it follows:

$$\mathbf{g} = \sum_s \dot{\gamma}_s \mathbf{R}_s. \tag{2}$$

According to our TEM investigations (Section 3), we consider four families of slip systems, reported in Table 2. For each family, a different stress sensitivity n^s was chosen to reproduce the variation of the macroscopic stress exponent for different textures and loading paths, as described in Section 3. It is worth mentioning that the obtained values ($n^{\mathrm{P}\langle\mathbf{a}\rangle} = 3$, $n^{\mathrm{B}\langle\mathbf{a}\rangle} = n^{\Pi_1\langle\mathbf{a}\rangle} = n^{\Pi_1\langle\mathbf{c}+\mathbf{a}\rangle} = 7$) lead to a physically relevant description of the slip systems activities [1]. Note that the secondary slip systems present the highest stress sensitivity. For the reference slip rate, the value $\dot{\gamma}_s^0 = 5 \times 10^{-7}\ \mathrm{s}^{-1}$ was adopted for all systems.

In order to obtain a correct description of the creep behaviour, it is required to take into account the intracrystalline hardening resulting from the interactions between the different slip systems. For that goal, the main difficulty comes from the several possible interactions in

Table 2
Slip systems in Zr alloys

Slip system	$\mathbf{n}_s$	$\mathbf{m}_s$
$\mathrm{P}\langle\mathbf{a}\rangle$	$\{10\bar{1}0\}$	$\langle1\bar{2}10\rangle$
$\Pi_1\langle\mathbf{a}\rangle$	$\{10\bar{1}1\}$	$\langle1\bar{2}10\rangle$
$\mathrm{B}\langle\mathbf{a}\rangle$	$\{0002\}$	$\langle1\bar{2}10\rangle$
$\Pi_1\langle\mathbf{c}+\mathbf{a}\rangle$	$\{10\bar{1}1\}$	$\langle\bar{2}113\rangle$

hexagonal crystals due to the crystalline geometry [19]. A phenomenological law accounting for self-hardening only leads to an unrealistic description of the behaviour [20]. An attempt to consider latent hardening has been made in [21] but results show a rather unrealistic activation of the secondary slip systems. On the other hand, the resort to a more 'physical' hardening law, like the one proposed by Essmann and Mughrabi [22] for FCC polycrystals, though promising, implies too many parameters to ensure a proper fitting operation on our experimental database. Owing to these remarks, we adopt in the following a phenomenological decription which captures the essential features of the intracrystalline hardening, namely the saturation of the reference shear stresses and the anisotropy of the interactions, similar to that used in [23] for a Zr-702 alloy. The form of this law, proposed by Kocks [24], reads

$$\dot{\tau}_s^0 = \sum_u H_0 \left(\frac{\tau_u^{\mathrm{sat}} - \tau_u^0}{\tau_u^{\mathrm{sat}} - \tau_u^{\mathrm{init}}} \right)^{a_{su}} Q_{su} |\dot{\gamma}_u| \tag{3}$$

with

$$Q_{su} = Q_0^{su} + (1 - Q_0^{su})\delta_{su}. \tag{4}$$

The coefficients H_0 and a_{su} describe the hardening kinetic. τ_u^{init} and τ_u^{sat} are, respectively, the initial and saturating reference shear stresses of system (u) and Q_0^{su} $(s \neq u)$ is the latent hardening coefficient between systems (s) and (u) ($Q_0^{su} = 1$ if $s = u$). It describes the anisotropy of the hardening in the material. A latent hardening stronger than self-hardening corresponds to $Q_0^{su} > 1$ $(s \neq u)$. It can be noted that relation (3) reduces to the 'physical' law of Essmann and Mughrabi [22] in the case of single slip with $a_{su} = 1$, $\forall s$, u (see, for instance, appendix of [25]). To the best of our knowledge, relatively few physical works have brought quantitative responses to the question of the latent hardening in zirconium alloys. To illustrate its complexity, it is worth to mention the work of Feaugas [26] who determined the result of the interactions between $\mathrm{P}\langle \mathbf{a} \rangle$ and $\Pi_1\langle \mathbf{a} \rangle$ slip systems (annihilation, creation of sessile or glissile junctions, etc.). Considering only these two families of slip leads to nine different interactions, that is nine different latent hardening terms in the hardening matrix. This would render the fitting procedure hardly manageable without further physical informations on these coefficients and it would be quite difficult to give an interpretation of the obtained values. As a consequence, a unique coefficient $Q_0 = Q_0^{su}$ $(s \neq u)$ is adopted to describe an average latent hardening in the material. For identical reasons, a sole nonlinear coefficient a was chosen.

4.2. Results

The parameters of the local behaviour have been identified by minimizing the discrepancy between the experimental macroscopic behaviour and the corresponding predictions of the micromechanical modelling. For that goal, we have used the 'Downhill Simplex' method [27] for which the derivative of the model response is not required. Besides, this method easily allows the minimization to be carried out with some constraints on the parameters, which are taken here as

$$\begin{cases} \tau^*_{\mathrm{P}\langle \mathbf{a} \rangle} = \min \tau_s^* \quad \text{with} \quad s = \Pi_1\langle \mathbf{a} \rangle, \Pi_1\langle \mathbf{c} + \mathbf{a} \rangle, \mathrm{B}\langle \mathbf{a} \rangle, \\ \tau^*_{\Pi_1\langle \mathbf{a} \rangle} < \tau^*_{\mathrm{B}\langle \mathbf{a} \rangle} < \tau^*_{\Pi_1\langle \mathbf{c}+\mathbf{a} \rangle}, \\ Q_0 \in [0; 3], \\ a \in [1; 3], \end{cases} \tag{5}$$

where the notation $*$ indicates that the condition holds for both initial and saturating reference shear stresses. The first condition implies that prismatic slip remains the easy-glide slip system. The second constraint reflects qualitatively our experimental TEM observations, i.e. a larger activation of $\Pi_1\langle \mathbf{a} \rangle$ as compared to $\mathrm{B}\langle \mathbf{a} \rangle$ and $\Pi_1\langle \mathbf{c} + \mathbf{a} \rangle$. The ranges fixed for the parameters Q_0 and a result from an analogy with the values usually reported for FCC polycrystals [28,29] in the absence of other physically based arguments. It can be remarked that we do not impose a priori a stronger latent hardening. To realize the identification of the parameters, the minimization has been performed using five experimental creep responses for each material resulting from different loading paths (axial and hoop tensile loadings, internal pressure) and stress levels (90–160 MPa).

The comparisons of the model with experimental macroscopic responses are illustrated in Figs. 13 and 14, respectively for uniaxial tension and internal pressure. It

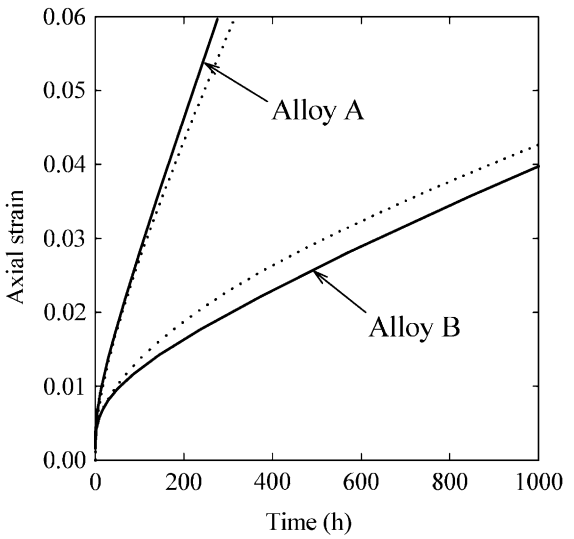

Fig. 13. Axial strain evolution during an uniaxial tensile creep test along AD ($T = 400$ °C, $\sigma_{zz} = 113$ MPa) for alloys A and B, simulation (continuous line), experiment (dotted line).

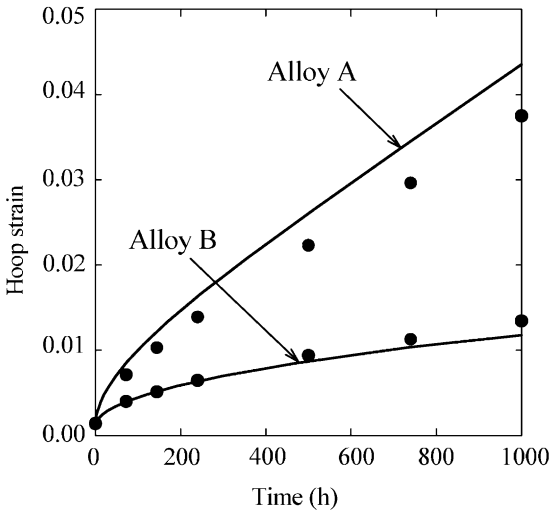

Fig. 14. Hoop strain evolution during an internal pressure creep test ($T = 400$ °C, $\sigma_{00} = 130$ MPa) for alloys A and B, simulation (continuous line), experiment (points).

can be seen that the creep behaviour is very well reproduced for the two alloys and the two different loading paths. It must be emphasized that the influence of the crystallographic texture (that is the anisotropy of the material) is nicely captured by the model. Uniaxial creep tests favor prismatic slip, whereas internal pressure tests tend to a higher activation of secondary slip systems, thus resulting to a much smaller deformation, as observed experimentally and by the simulation. One important result of the identification procedure is that we obtain for both alloys the same parameters $a = 1.5$ and $H_0 = 375$ MPa for the description of the hardening kinetic. This result is consistent with the experimental evidence that niobium in solid solution does not affect the involved slip modes (Section 3). The same type of dislocation interactions can thus be expected in both alloys. Besides, a stronger latent than self-hardening is obtained with again a unique Q_0 value ($Q_0 = 1.9$) for both alloys, which is close to the one observed experimentally for two prismatic slip systems [30]. The values of the initial and saturating reference shear stresses for alloys A and B are reported in Table 3. It is observed

Table 3
Initial and saturating reference shear stresses for Zr–Nb1%–O alloys A and B

	P$\langle \mathbf{a} \rangle$	$\Pi_1\langle \mathbf{a} \rangle$	B$\langle \mathbf{a} \rangle$	$\Pi_1\langle \mathbf{c}+\mathbf{a} \rangle$
Alloy A				
τ^{init} (MPa)	31	59	62	136
τ^{sat} (MPa)	63	84	86	150
Alloy B				
τ^{init} (MPa)	41	62	89	176
τ^{sat} (MPa)	90	93	134	200

that the ratio $\tau^{\text{sat}}/\tau^{\text{init}}$, for a given slip mode, is almost invariant between alloys A and B. This is consistent with the unique hardening kinetic found above and with TEM observations showing identical activations of slip systems in both alloys. The identification leads to an increase of the initial and saturating reference shear stresses in alloy B for all slip systems and particularly it can be noted that a gap of about 30 MPa, between both alloys, for the saturating value of the prismatic reference shear stress is obtained. This variation of the reference shear stresses between both alloys represents in a phenomenological way the solid solution hardening which has been shown to be the predominant mechanism (see Section 3). The gap of about 30 MPa is in good agreement with the hardening exhibited at low strain rates (Fig. 12(a)). Therefore, although relations (1) and (3) clearly present a phenomenological aspect, the obtained parameters reconcile an accurate prediction of the effective responses and a correct description of the local physical deformation processes. This result is confirmed by a recent analysis of residual stresses by neutron diffraction [31]. Interestingly, it can be noted that the hardening kinetic obtained for Zr–Nb1%–O alloy is very similar to the one reported by Castelnau et al. [23] for the behaviour of Zr 702 alloy at large strain and Brenner [1] for the thermal creep of Zircaloy-4, in the 'low temperature' domain ($T/T_m \leqslant 0.3$ with T_m the melting temperature). This result tends to show that, in this temperature range, the *interactions* between different slip systems are rather independent on the chemical composition for these usual Zr alloys.

5. Conclusion

The creep responses of two Zr–Nb1%–O alloys have been investigated in details. The two alloys exhibit identical crystallographic textures, grain size, grain shape, and chemical composition. They *only* differ by the thermal cycles during the elaboration process, alloy A being elaborated at low temperature whereas for alloy B thermal treatments alternate below and above the monotectoïd temperature. It has been shown that alloy B deforms by creep about 4 times slower than alloy A. Mechanical tests and TEM observations show that this difference cannot be attributed to the alignment of the β-Nb precipitate phase observed in alloy B. Additional heat treatments, combined with an X-ray analysis, show that alloy B is not in a thermodynamical stable state, due to the slow precipitation kinetic of the β-Nb phase during cooling. This result is confirmed by the creep response of the heat-treated alloy B, which presents a viscosity intermediate between alloy A and B in their initial state, and by TEM X-ray spectrometry which gives a higher Nb content of about 0.1% in the α-Zr phase for alloy B. Our results thus strongly suggest a

hardening effect due to solute Nb atoms in the α-Zr matrix to explain the differences between both alloys. The applied scale-transition model, based on an affine formulation for non-linear elastoviscoplastic behaviour, has been shown to capture properly the dependence of the creep response on the loading path direction. The parameters of the local constitutive relation, including an anisotropic and saturating hardening law, are in good agreement with the experimental observations and describe phenomenologically the microstructural effects observed. In particular, we found out that both alloys present an identical hardening kinetic, a result consistent with the experimental evidence that different Nb contents in solid solution does not affect the involved slip systems. Alloy B exhibit a saturating reference shear stress for prismatic slip about 30 MPa higher than alloy A.

Acknowledgements

This work was partially supported by EdF and Framatome ANP Nuclear Fuel, and the cladding tubes were provided by Framatome ANP Zircotube. The authors wish to thank J.P. Mardon (Framatome ANP Nuclear Fuel) for fruitful discussions and express their gratitude to F. Gregori (LPMTM, CNRS) for her generous contribution to the TEM observations.

Appendix A. Micromechanical model for heterogeneous elastoviscoplastic materials

Let us assume that the average strain rate $\dot{\boldsymbol{\varepsilon}}_r$ in a phase (r) at a given time t is given by

$$\dot{\boldsymbol{\varepsilon}}_r(t) = \mathbf{s} : \dot{\boldsymbol{\sigma}}_r(t) + \mathbf{g}(\boldsymbol{\sigma}_r(t)) \tag{A.1}$$

with $\boldsymbol{\sigma}_r$ and $\dot{\boldsymbol{\sigma}}_r$, respectively, the average stress and stress rate in phase (r), $\mathbf{s}$ the elastic compliance and $\mathbf{g}$ the viscoplastic flow law. Note that here, $\mathbf{g}$ only results from the physical process of dislocation glide on particular crystallographic planes, but in a more general problem, $\mathbf{g}$ can also account for irradiation creep and growth with no additional difficulties. To be able to apply classical homogenization tools, it is necessary to linearize relation (A.1). Following [15], the linearized form of $\dot{\boldsymbol{\varepsilon}}_r(t)$ is given, for any time t and a given linearization time ζ, by

$$\dot{\boldsymbol{\varepsilon}}_r(t) = \mathbf{s} : \dot{\boldsymbol{\sigma}}_r(t) + \mathbf{m}(\boldsymbol{\sigma}_r(\zeta)) : \boldsymbol{\sigma}_r(t) + \dot{\boldsymbol{\varepsilon}}^0_r(\zeta, t) \tag{A.2}$$

with $\mathbf{m} = \partial\mathbf{g}/\partial\boldsymbol{\sigma}$. Roughly speaking, (A.2) is an affine linearization of the local behaviour (A.1) incorporating the hereditary nature inherent to the elastoviscoplastic behaviour. The linearized behaviour can be written in the more convenient form of a Stieljes convolution product denoted $*$, i.e.

$$\begin{aligned} &\boldsymbol{\varepsilon}(t) = \mathbf{q}(\zeta, t) * \boldsymbol{\sigma}(t) + \boldsymbol{\varepsilon}^0(\zeta, t), \\ &\mathbf{q}(\zeta, t) = \mathbf{s} + \mathbf{m}(\zeta)t. \end{aligned} \tag{A.3}$$

The obtained linear constitutive law is thus of (linear) maxwellian type with eigenstrain. To obtain the homogenized properties at time $t = \zeta$, the correspondence principle [32] can be applied. For that goal, the use of the Laplace–Carson (LC) transform of (A.3) is particularly convenient. It leads to

$$\begin{aligned} &\hat{\boldsymbol{\varepsilon}}_r(p) = \hat{\mathbf{q}}(\zeta, p) : \hat{\boldsymbol{\sigma}}_r(p) + \hat{\boldsymbol{\varepsilon}}^0_r(\zeta, p), \\ &\hat{\mathbf{q}}(\zeta, p) = \mathbf{s} + \frac{1}{p}\mathbf{m}(\zeta), \end{aligned} \tag{A.4}$$

where $\hat{f}$ denotes the transform of the function f and p is the complex variable. In the LC space, (A.4) thus defines a symbolic thermoelastic behaviour to which homogenization schemes apply. The effective symbolic compliance $\widehat{\mathbf{Q}}$ and eigenstrain $\widehat{\mathbf{E}}^0$ are thus classically given by

$$\begin{cases} \widehat{\mathbf{Q}}(\zeta, p) = \left\langle \hat{\mathbf{q}}(\zeta, p) : \widehat{\mathbf{B}}_r(\zeta, p) \right\rangle, \\ \widehat{\mathbf{E}}^0(\zeta, p) = \left\langle {}^t\widehat{\mathbf{B}}_r(\zeta, p) : \hat{\boldsymbol{\varepsilon}}^0_r(\zeta, p) \right\rangle, \end{cases} \tag{A.5}$$

where $\widehat{\mathbf{B}}_r$ is the symbolic stress average concentration tensor over phase r. It can be determined using the Eshelby's solution of the inclusion problem [13]. Regarding the 'granular' microstructure of the polycrystal, i.e. all the phases are on the same footing, the self-consistent scheme is applied. It implies that each inclusion is embedded in an infinite medium whose compliance is the one of the homogeneous equivalent material. Finally, it is necessary to perform the inversion of the obtained symbolic responses $\hat{\boldsymbol{\sigma}}_r$ and $\hat{\boldsymbol{\varepsilon}}_r$. In our approach, we approximate this inversion using a generalization of the work of Schapery [33]. It is emphasized that this scheme differs, as explained in [17], from the former approach of Turner et al. [34] for the description of both transient and steady-state regimes. Particularly, it can be noted that this earlier proposition was restricted to power-law viscoplastic flow rule with an uniform stress sensitivity in the material.

References

[1] R. Brenner, PhD thesis, Université Paris XIII, 2001.
[2] R. Brenner, J.-L. Béchade, B. Bacroix, Proc. 12th Int. Conf. Textures Mater., Montreal, Canada, 9–13 August, NRC Research, 1999.
[3] J.P. Mardon, D. Charquet, J. Sénevat, 12th Int. Symp. Zirconium Nucl. Indus., Toronto, Canada, 10–14 June, ASTM-STP 1354, 1998.
[4] T.B. Massalski, J.L. Muryay, L.H. Bennett, H. Baker, Binary Alloy Phase Diagrams, ASM International, Materials Park, OH, 1986.
[5] E. Tenckhoff, Deformation Mechanisms, Texture and Anisotropy in Zirconium and Zircaloy, ASTM-STP 966, Philadelphia, PA, 1988.

[6] P.G. Partridge, Met. Rev. 118 (1967) 169.
[7] C. Toffolon, J.C. Brachet, T. Guilbert, D. Hamon, S. Urvoy, C. Servant, D. Charquet, L. Legras, J.P. Mardon, J. Phys. IV 81 (2001) 99.
[8] S.A. Aldridge, B.A. Cheadle, J. Nucl. Mater. 42 (1972) 32.
[9] J. Friedel, Dislocations, Pergamon, 1964.
[10] R.L. Fleisher, J. Appl. Phys. 33 (1962) 3504.
[11] U.F. Kocks, C.N. Tomé, H.R. Wenk, Texture and Anisotropy, Cambridge University, 1998.
[12] M. Bornert, T. Bretheau, P. Gilormini, Homogénéisation en mécanique des matériaux, Hermès Science, Paris, France, 2001.
[13] J.D. Eshelby, Proc. R. Soc. Lond. A 241 (1957) 376.
[14] A. Zaoui, J.L. Raphanel, in: T.C. Lowe, A.D. Rollett, P.S. Follansbee, G.S. Daehn (Eds.), Modeling the Deformation of Crystalline Solids, TMS, 1991, p. 51.
[15] R. Masson, A. Zaoui, J. Mech. Phys. Solids 47 (1999) 8543.
[16] A. Pouya, A. Zaoui, C.R. Acad. Sci. Paris sér. IIb 327 (1999) 365.
[17] R. Brenner, R. Masson, O. Castelnau, A. Zaoui, Eur. J. Mech. A/Solids, in press.
[18] P. Delobelle, P. Robinet, P. Geyer, P. Bouffioux, J. Nucl. Mater. 238 (1996) 135.
[19] G.J. Weng, Int. J. Plast. 3 (1987) 315.
[20] A.A. Pochettino, P. Sanchez, Proc. 12th Int. Conf. Textures Mater., Montreal, Canada, 9–13 August, NRC Research, 1999.
[21] P.J. Maudlin, C.N. Tomé, G.C. Kaschner, G.T. Gray, Proc. 6th Int. Conf. Numer. Meth. Indus. Forming Process., University of Twente, Enschede, 1998.
[22] U. Essmann, H. Mughrabi, Phil. Mag. A. 40 (1979) 731.
[23] O. Castelnau, H. Francillette, B. Bacroix, R.A. Lebensohn, J. Nucl. Mater. 297 (2001) 14.
[24] U.F. Kocks, J. Eng. Mater. Tech. 10 (1976) 76.
[25] A. Paquin, S. Berbenni, V. Favier, X. Lemoine, M. Berveiller, Int. J. Plast. 17 (2001) 1267.
[26] X. Feaugas, PhD thesis, Université Technologique de Compiègne, 1994.
[27] W. Press, B. Flannery, S. Teukolsky, W. Vetterling, Numerical Recipes – The Art of Scientific Computing, Cambridge University, 1986.
[28] C.A. Bronkhorst, S.R. Kalidindi, L. Anand, Proc. R. Soc. Lond. A 341 (1992) 443.
[29] S. Balasubramanian, L. Anand, J. Mech. Phys. Solids 50 (2002) 101.
[30] J. Crepin, personal communication, 2002.
[31] N. Letouzé, R. Brenner, O. Castelnau, J.-L. Béchade, M.-H. Mathon, Scripta Mater., in press.
[32] J. Mandel, Mécanique des milieux continus, Gauthier-Villars, Paris, 1966.
[33] R.A. Schapery, Proc. US Nat. Congr. Appl. Mech. ASME 4th, 1962.
[34] P.A. Turner, C.N. Tomé, C. Woo, Philos. Mag. A 70 (1994) 689.